

Parameterized Principal Component Analysis

Ajay Gupta^a, Adrian Barbu^{a,*}

^a*Department of Statistics, Florida State University, USA*

Abstract

When modeling multivariate data such as vectorized images, one might have an extra parameter of contextual information that could be used to treat some observations as more similar to others. For example, images of faces can vary by yaw rotation, and one would expect a face rotated 65° to the left to have characteristics more similar to a face rotated 55° to the left than to a face rotated 65° to the right. We introduce a novel method, parameterized principal component analysis (PPCA), that can model data with linear variation like principal component analysis (PCA), but can also take advantage of this parameter of contextual information like yaw rotation.

Like PCA, PPCA models an observation using a mean vector and the product of observation-specific coefficients and basis vectors. Unlike PCA, PPCA treats the elements of the mean vector and basis vectors as smooth, piecewise linear functions of the contextual parameter. PPCA is fit by a penalized optimization that penalizes potential models which have overly large differences between corresponding mean or basis vector elements for similar parameter values. The penalty ensures that each observation's projection will share information with observations that have similar parameter values, but not with observations that have dissimilar parameter values.

We tested PPCA on artificial data based on known, smooth functions of an added parameter, as well as on three real datasets with different types of

*Corresponding author.

Email address: abarbu@stat.fsu.edu (Adrian Barbu)

URL: <http://stat.fsu.edu/~abarbu/> (Adrian Barbu)

parameters. We compared PPCA to independent principal component analysis (IPCA), which groups observations by their parameter values and projects each group using principal component analysis with no sharing of information for different groups. PPCA recovers the known functions with less error and projects the datasets’ test set observations with consistently less reconstruction error than IPCA does. PPCA’s performance is particularly strong, relative to IPCA, when there are limited training data.

Keywords: Manifold learning, Multivariate data, Context, Face modeling, Principal component analysis, Subspaces

1. Introduction

In recent years, storing and modeling multidimensional data have become very common. Potential datasets include different attributes of potential customers, multiple currencies’ exchange rates for each day, and vectorized images. Although these data often lie on non-linear manifolds, a linear manifold or a combination of linear manifolds can often provide a practical and suitably accurate approximation. Particularly for data of very high dimensionality such as vectorized images, a model may need to produce a reduced-dimension representation of the original observations. One particularly effective technique for modeling linear manifolds and incorporating dimensionality reduction is principal component analysis (PCA), which finds a basis \mathbf{P} of vectors that can capture the highest-variance directions from the original data [10].

Pitelis et al. (2013) showed how an “atlas” of overlapping linear manifolds that they labeled “charts” could model a non-linear manifold very effectively [12]. Their model was learned by a hill-climbing approach which alternated between assigning observations to charts based on the observations’ values and refitting each chart using PCA performed on the relevant subset of observations. The initial charts, which were necessary for the first assignments, could be found by PCA on bootstrap samples. The number of charts was selected by the method based on a user-supplied penalty λ .

Vidal, Ma, and Sastry (2005) introduced Generalized Principal Component Analysis (GPCA), which similarly addressed the idea of dividing a larger manifold into multiple local manifolds. GPCA used polynomials based on Veronese maps to modify and combine elements of the original data vectors. GPCA could still learn the coefficients of the monomial terms by PCA, though, because the relationship between the full polynomial and these coefficients was still linear [14]. The experimental success of GPCA showed that multiple applications of (linear) PCA could be used to learn a complicated manifold, although the local manifolds learned were typically non-linear. The authors noted, though, that piecewise linear models (which could be learned by multiple PCA applications without GPCA’s polynomials) are “excellent” in many practical applications at balancing the need for model expressiveness with the desire for model simplicity [13]. Like the atlas method, GPCA could also select the appropriate number of local manifolds, but using the ranks of Veronese maps evaluated on the observations instead of user-supplied parameters [14].

Techniques such as GPCA and the atlas-based method exist for identifying local manifolds for observations based on the observations’ values, and for identifying the number of local manifolds. Situations exist, however, in which data are thought to lie approximately on local manifolds that estimate a larger manifold, but one knows which local manifold corresponds to each observation instead of needing the algorithm to discover this. For example, one may be modeling images of vehicles using a known class (“car,” “motorcycle,” “SUV,” or “truck”) for each observation. Linear discriminant analysis (LDA) uses linear manifolds to perform dimensionality reduction in a scenario with such classes. However, LDA chooses its basis vectors based on what can separate classes rather than what can capture the variation of each class [10]. Other techniques such as Class-Information-Incorporated Principal Component Analysis [3], Joint Parameterized Atom Selection [15], Locality Preserving Projections [8], Multi-Manifold Semi-Supervised Learning [6], Multimodal Oriented Discriminant Analysis [5], and Semi-Supervised Dimensionality Reduction [17] learn manifolds in the presence of subspaces or classes. Like LDA, however, these are

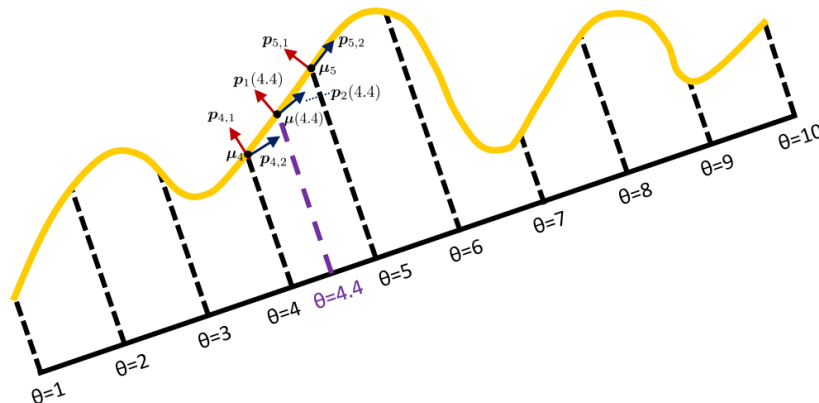
focused on classification to a local manifold rather than focused on modeling the observations once the classes are known.

One reason that modeling known classes has been effectively unaddressed is that one could treat the modeling problem as many separate problems, each of which could be addressed by existing techniques such as PCA. For notational simplicity, we will refer to the use of a separate PCA model for each group as Independent Principal Component Analysis (IPCA), because none of the classes' models use information from the other classes' observations. If one had a quantitative "parameter" rather than categories to determine the local manifold, one would perform IPCA by forming histogram-like bins and running one PCA model per bin.

Various applications exist in which this extra contextual information would be quantitative. For vehicle images, one could model them differently based on the vehicles' weights, volumes, or prices (MSRPs). Daily percent changes in a stock's closing share price could use the stock's market capitalization, because smaller-capitalization stocks are thought to have more volatile price movements. Lenders with multiple recorded attributes about their borrowers could use the borrowers' rates of interest or FICO credit scores as the parameters.

This contextual parameter carries ordinal and interval information that would be ignored by IPCA. Consider borrower data such as a borrower's number of late payments, with credit scores as the parameter, and bins 300-350, 350-400, and so on until 800-850. The average late payments might decrease in the training examples as the bin increases, except that the 400-450 bin might have a surprisingly low average. IPCA would ignore the other bins and the pattern they form, which could overfit the training examples in the 400-450 bin. Additionally, IPCA would treat customers with credit scores of 355 and 845 as completely different from one with a credit score of 345, because all three are in different bins. It would ignore that the difference between 345 and 355 is much smaller than the difference between 345 and 845, rather than enforcing similarity between how the 345-score and 355-score observations are modeled.

In this paper, we propose a new method called parameterized principal com-



ponent analysis (PPCA) for creating a PCA-like linear model for multivariate data that are associated with a separate parameter with known, observation-specific values. Like IPCA, PPCA makes multiple linear models of mean vectors and bases, which are based on known divisions of the parameter space. Unlike IPCA, PPCA interpolates between the points in the parameter space at which mean vectors and bases were fitted, and penalizes differences in the models for similar parameter values. We describe the PPCA model in Section 2, and discuss its implementation in Sections 3 and 4. In Section 5, we apply PPCA to artificial data following smooth functions of the parameter, and to three real datasets: shapes of differently-sized lymph nodes, human facial images with different degrees of added blurriness, and human facial images with different angles of yaw rotation. In all four experiments, PPCA outperformed IPCA, and was particularly beneficial when the number of training examples was limited.

2. Parameterized Principal Component Analysis

Parameterized principal component analysis (PPCA) applies to an environment in which there are n observations \mathbf{x}_i , each of dimension K , and there are B bin endpoints arising from the $B - 1$ bins that partition the acceptable range of the parameter θ . Each bin endpoint b has a mean vector $\boldsymbol{\mu}_b$ and V basis vectors $\mathbf{p}_{b,v}$. Each bin endpoint corresponds to a value of θ , and an observation

\mathbf{x}_i 's parameter value θ_i dictates \mathbf{x}_i 's bin, with lower endpoint $b_{(l),i}$ and upper endpoint $b_{(u),i}$. Figure 1 shows an example using a parameter that varies from $\theta = 1$ to $\theta = 10$. Note that a bin endpoint usually applies to two bins. For the example in Figure 1, the bin endpoint at $\theta = 3$ would be an endpoint for the 2-3 bin and for the 3-4 bin.

The parameter θ_i can be translated into weights $w_l(\theta_i)$ and $w_u(\theta_i)$ for bin endpoints $b_{(l),i}$ and $b_{(u),i}$. Equation (1) shows this, using $\theta_l(\theta_i)$ and $\theta_u(\theta_i)$ as the parameter values for the bin's lower and upper endpoint, respectively. Figure 2 shows an example for an observation with $\theta_i = 4.4$. It has a 60% weight for the bin endpoint at $\theta = 4$ and a 40% weight for the bin endpoint at $\theta = 5$, because 4.4 is 60% of the way from 5 to 4, and 40% of the way from 4 to 5.

$$w_l(\theta_i) = \frac{\theta_u(\theta_i) - \theta_i}{\theta_u(\theta_i) - \theta_l(\theta_i)}, w_u(\theta_i) = \frac{\theta_i - \theta_l(\theta_i)}{\theta_u(\theta_i) - \theta_l(\theta_i)} \quad (1)$$

These weights can produce a mean vector $\boldsymbol{\mu}(\theta_i)$ and a basis $\mathbf{P}(\theta_i)$ that are specific to the observation's parameter θ_i , as shown in Equations (2) and (3).

$$\boldsymbol{\mu}(\theta_i) = w_l(\theta_i)\boldsymbol{\mu}_{b_{(l),i}} + w_u(\theta_i)\boldsymbol{\mu}_{b_{(u),i}} \quad (2)$$

$$\mathbf{P}(\theta_i) = w_l(\theta_i) \begin{bmatrix} \mathbf{p}_{b,1} & \mathbf{p}_{b,2} & \cdots & \mathbf{p}_{b,V} \end{bmatrix} + w_u(\theta_i) \begin{bmatrix} \mathbf{p}_{b+1,1} & \mathbf{p}_{b+1,2} & \cdots & \mathbf{p}_{b+1,V} \end{bmatrix} \quad (3)$$

The model produces a lower-dimensional representation of \mathbf{x}_i as the coefficient vector $\boldsymbol{\beta}_i$. This can be translated to a projection of \mathbf{x}_i using $\boldsymbol{\mu}(\theta_i) + \mathbf{P}(\theta_i)\boldsymbol{\beta}_i$.

2.1. Energy Function

PPCA uses the minimization of an energy function $E(\cdot)$ to achieve a balance between having these projections fit the training examples well and reducing differences between adjacent bin endpoints' corresponding model components.

$$E(\boldsymbol{\mu}, \mathbf{p}, \boldsymbol{\beta}, \lambda_{r,m}, \lambda_{r,v}, \lambda_o) = E_{\text{data}}(\boldsymbol{\mu}, \mathbf{p}, \boldsymbol{\beta}) + E_{\text{rough.}}(\boldsymbol{\mu}, \mathbf{p}, \lambda_{r,m}, \lambda_{r,v}) + E_{\text{ortho.}}(\mathbf{p}, \lambda_o) \quad (4)$$

Equation (4) uses the vectors $\boldsymbol{\mu}$, \boldsymbol{p} , and $\boldsymbol{\beta}$, which are stacked from vectors introduced earlier, as detailed in Equation (5). The functions $\boldsymbol{\mu}(\theta_i)$ and $\boldsymbol{P}(\theta_i)$ can be derived from the vectors $\boldsymbol{\mu}$ and \boldsymbol{p} , and the coefficient vectors $\boldsymbol{\beta}_i$ can be extracted from $\boldsymbol{\beta}$.

$$\boldsymbol{\mu} = \begin{bmatrix} \boldsymbol{\mu}_1 \\ \boldsymbol{\mu}_2 \\ \vdots \\ \boldsymbol{\mu}_B \end{bmatrix}, \boldsymbol{p} = \begin{bmatrix} \boldsymbol{p}_{1,1} \\ \boldsymbol{p}_{1,2} \\ \vdots \\ \boldsymbol{p}_{1,V} \\ \boldsymbol{p}_{2,1} \\ \vdots \\ \boldsymbol{p}_{B,V-1} \\ \boldsymbol{p}_{B,V} \end{bmatrix}, \boldsymbol{\beta} = \begin{bmatrix} \boldsymbol{\beta}_1 \\ \boldsymbol{\beta}_2 \\ \vdots \\ \boldsymbol{\beta}_n \end{bmatrix} \quad (5)$$

The first term within the energy function in Equation (4) is $E_{\text{data}}(\cdot)$, which is detailed in Equation (6). $E_{\text{data}}(\cdot)$ is the mean ℓ_2 norm of the training examples' approximation errors, using the model's current representation of all training examples' $\boldsymbol{\mu}(\theta_i)$, $\boldsymbol{P}(\theta_i)$, and $\boldsymbol{\beta}_i$.

$$E_{\text{data}}(\boldsymbol{\mu}, \boldsymbol{p}, \boldsymbol{\beta}) = \frac{1}{n} \sum_{i=1}^n \|\boldsymbol{x}_i - \boldsymbol{\mu}(\theta_i) - \boldsymbol{P}(\theta_i)\boldsymbol{\beta}_i\|^2 \quad (6)$$

The second term from $E(\cdot)$, $E_{\text{rough}}(\cdot)$, is shown in Equation (7). It uses the penalty coefficients $\lambda_{r,m}$ and $\lambda_{r,v}$ to ensure smooth functions for the mean vectors and basis vectors, respectively. Differences between corresponding elements for vectors relevant to two endpoints of the same bin are penalized.

$$E_{\text{rough}}(\boldsymbol{\mu}, \boldsymbol{p}, \lambda_{r,m}, \lambda_{r,v}) = \frac{\lambda_{r,m}}{B-1} \sum_{b=1}^{B-1} \|\boldsymbol{\mu}_b - \boldsymbol{\mu}_{b+1}\|^2 + \frac{\lambda_{r,v}}{B-1} \sum_{b=1}^{B-1} \sum_{v=1}^V \|\boldsymbol{p}_{b,v} - \boldsymbol{p}_{b+1,v}\|^2 \quad (7)$$

Large values of $\lambda_{r,m}$ and $\lambda_{r,v}$ will enforce more smoothness in the representation, at the expense of the projection error on the training set.

PPCA's two roughness penalty coefficients $\lambda_{r,m}$ and $\lambda_{r,v}$ force the model for an observation to incorporate information from observations with similar

observations: those in its bin and those in the adjacent bin(s). The amount of the information sharing depends on the differences in parameter values, even for observations in the same bin. The weighted pooling of information enforces a prior belief that observations with more similar values of a parameter should be modeled in a more similar manner. It enforces smoothness, but not monotonicity. Ordinal trends can still be captured, but only locally. This gives PPCA the ability to approximate more complicated smooth functions, though, such as sinusoidal curves. Like the prior beliefs in Bayesian models, PPCA’s prior belief is more useful in the presence of limited training data, because the pooling of information can reduce overfitting.

The energy function also includes the Lagrange multiplier $E_{\text{ortho.}}$, which is illustrated in Equation (8). In Equation (8), the functions $\mathbf{1}_{(v=w)}$ are indicators for the condition $v = w$.

$$E_{\text{ortho.}}(\mathbf{p}, \lambda_o) = \lambda_o \sum_{b=1}^B \sum_{v=1}^V \sum_{w=v}^V (\langle \mathbf{p}_{b,v}, \mathbf{p}_{b,w} \rangle - \mathbf{1}_{(v=w)})^2 \quad (8)$$

$E_{\text{ortho.}}(\cdot)$ encourages orthonormality in each bin endpoint’s basis. It penalizes differences from zero for dot products of pairs of vectors from the same bin, promoting orthogonality of each basis. It also penalizes differences from one for the squared ℓ_2 norm of each vector.

3. Learning a Parameterized Principal Component Analysis Model

Because the energy function is composed of quadratic terms, we assume it to be locally convex. We find a local minimum in the energy function using partial derivatives of the energy function with respect to the stacked mean vector $\boldsymbol{\mu}$, the stacked basis vector \mathbf{p} , and each observation’s coefficient vector $\boldsymbol{\beta}_i$. We either perform gradient descent or set the derivative to the zero vector and solved for the model component being optimized.

PPCA needs to choose optimal vectors $\boldsymbol{\mu}$, \mathbf{p} , and $\boldsymbol{\beta}$, and a derivative-based method for one of the three requires knowing or estimating the other two. In PPCA, we optimize one at a time, holding the other two as constant vectors

based on their most recent estimates. After initialization, we run several cycles of optimizing the mean vectors, followed by the basis vectors, and then the coefficient vectors. We choose a pre-determined number of cycles n_c , and terminate the algorithm early if the algorithm is deemed to have converged, based on the energy. We store one previous iteration's estimates of the model components $\boldsymbol{\mu}$, \mathbf{p} , and $\boldsymbol{\beta}$, so these estimates can be treated as final if the energy increases.

3.1. Learning Mean Vectors

A closed-form solution for $\hat{\boldsymbol{\mu}}$, the PPCA estimate of $\boldsymbol{\mu}$, is displayed in Equation (9). This uses the observation-specific matrix \mathbf{W}_i from Equation (10), which is made up of bin endpoint weights $w_{b,i}$. The weight $w_{b,i}$ is equal to $w_l(\theta_i)$ if b is the lower endpoint for observation i , $w_u(\theta_i)$ if b is upper endpoint for observation i , and zero otherwise. Equation (9) also uses the weight-product matrix $\mathbf{C}_{(M),i}$ from Equation (11) and the matrix $\mathbf{R}_{(M)}$ from Equation (12). $\mathbf{R}_{(M)}$ has only three diagonals of non-zero elements, all of which are -1, 1, or 2.

$$\hat{\boldsymbol{\mu}} = \frac{1}{n} \left(\frac{1}{n} \sum_{i=1}^n [\mathbf{C}_{(M),i}] + \frac{\lambda_{r,m}}{B-1} \mathbf{R}_{(M)} \right)^{-1} \sum_{i=1}^n (\mathbf{W}_i^T [\mathbf{x}_i - \mathbf{P}(\theta_i) \boldsymbol{\beta}_i]) \quad (9)$$

$$\mathbf{W}_i = \begin{bmatrix} w_{1,i} I_K & w_{2,i} I_K & \cdots & w_{B,i} I_K \end{bmatrix} \quad (10)$$

$$\mathbf{C}_{(M),i} = \begin{bmatrix} w_{1,i}^2 I_K & w_{1,i} w_{2,i} I_K & \cdots & w_{1,i} w_{B,i} I_K \\ w_{2,i} w_{1,i} I_K & w_{2,i}^2 I_K & \cdots & w_{2,i} w_{B,i} I_K \\ \vdots & \vdots & \ddots & \vdots \\ w_{B,i} w_{1,i} I_K & w_{B,i} w_{2,i} I_K & \cdots & w_{B,i}^2 I_K \end{bmatrix} \quad (11)$$

$$\mathbf{R}_{(M)} = \begin{bmatrix} I_K & -I_K & \mathbf{0}_{K \times K} & \cdots & \mathbf{0}_{K \times K} & \mathbf{0}_{K \times K} & \mathbf{0}_{K \times K} \\ -I_K & 2I_K & -I_K & \cdots & \mathbf{0}_{K \times K} & \mathbf{0}_{K \times K} & \mathbf{0}_{K \times K} \\ \mathbf{0}_{K \times K} & -I_K & 2I_K & \cdots & \mathbf{0}_{K \times K} & \mathbf{0}_{K \times K} & \mathbf{0}_{K \times K} \\ \vdots & \vdots & \vdots & \ddots & \vdots & \vdots & \vdots \\ \mathbf{0}_{K \times K} & \mathbf{0}_{K \times K} & \mathbf{0}_{K \times K} & \cdots & 2I_K & -I_K & \mathbf{0}_{K \times K} \\ \mathbf{0}_{K \times K} & \mathbf{0}_{K \times K} & \mathbf{0}_{K \times K} & \cdots & -I_K & 2I_K & -I_K \\ \mathbf{0}_{K \times K} & \mathbf{0}_{K \times K} & \mathbf{0}_{K \times K} & \cdots & \mathbf{0}_{K \times K} & -I_K & I_K \end{bmatrix} \quad (12)$$

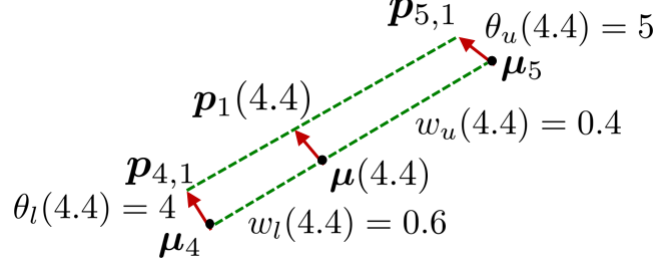


Figure 2: Example of Combination from Bin Endpoint Weights

The use of a matrix inverse or linear system solution for $\hat{\boldsymbol{\mu}}$ is either impractically slow or inaccurate for high-dimensional data such as vectorized images. For these data, we optimized the mean vectors using a gradient descent algorithm and the energy derivative from Equation (13).

$$\frac{\partial E}{\partial \boldsymbol{\mu}} = -\frac{2}{n} \sum_{i=1}^n [C_{(M),i}(\mathbf{y}_i - \boldsymbol{\mu} - \mathbf{B}_i \mathbf{p})] + \frac{2\lambda_{r,m}}{B-1} \mathbf{R}_{(M)} \boldsymbol{\mu} \quad (13)$$

Equation (13) uses the observation-specific coefficient matrices \mathbf{B}_i , which are defined using Equations (14) and (15). It also uses the stacked vectors \mathbf{y}_i , which stack B identical copies of an observation \mathbf{x}_i .

$$\mathbf{B}_i = \begin{bmatrix} \mathbf{B}_{(B),i} & \mathbf{0}_{K \times KV} & \cdots & \mathbf{0}_{K \times KV} \\ \mathbf{0}_{K \times KV} & \mathbf{B}_{(B),i} & \cdots & \mathbf{0}_{K \times KV} \\ \vdots & \vdots & \ddots & \vdots \\ \mathbf{0}_{K \times KV} & \mathbf{0}_{K \times KV} & \cdots & \mathbf{B}_{(B),i} \end{bmatrix}_{BK \times BKV} \quad (14)$$

$$\mathbf{B}_{(B),i} = \begin{bmatrix} \beta_{i,1} I_K & \beta_{i,2} I_K & \cdots & \beta_{i,V} I_K \end{bmatrix}_{K \times KV} \quad (15)$$

3.2. Learning Basis Vectors

We only use gradient descent to optimize \mathbf{p} , because the presence of a dot product within a quadratic term creates a quartic term that prevents a closed-form solution. The derivative is in Equation (16), and it relies on the BKV -

length vectors \mathbf{b}_i , which stack products of the weights, coefficients, and residuals.

$$\frac{\partial E}{\partial \mathbf{p}} = -\frac{2}{n} \sum_{i=1}^N \mathbf{b}_i + \left(\frac{\lambda_{r,v}}{B-1} \mathbf{R}_{(V)} - 4\lambda_{r,v} \right) \mathbf{p} + 2\lambda_o \sum_{b=1}^B \sum_{v=1}^{V_b} \sum_{w=v}^{V_b} [(\mathbf{T}_{b,v,w} + \mathbf{T}_{b,w,v}) \mathbf{p} \mathbf{p}^T \mathbf{T}_{b,w,v} \mathbf{p}] \quad (16)$$

$$\mathbf{b}_i = \begin{bmatrix} w_{1,i} \beta_{i,1} [\mathbf{x}_i - \boldsymbol{\mu}(\theta_i) - \mathbf{P}(\theta_i) \boldsymbol{\beta}_i] \\ w_{1,i} \beta_{i,2} [\mathbf{x}_i - \boldsymbol{\mu}(\theta_i) - \mathbf{P}(\theta_i) \boldsymbol{\beta}_i] \\ \vdots \\ w_{B,i} \beta_{i,V-1} [\mathbf{x}_i - \boldsymbol{\mu}(\theta_i) - \mathbf{P}(\theta_i) \boldsymbol{\beta}_i] \\ w_{B,i} \beta_{i,V} [\mathbf{x}_i - \boldsymbol{\mu}(\theta_i) - \mathbf{P}(\theta_i) \boldsymbol{\beta}_i] \end{bmatrix} \quad (17)$$

Equation (16) also uses the transition-like matrix $\mathbf{T}_{b,v,w}$ from Equation (18) and the bin-comparison matrix $\mathbf{R}_{(V)}$ from Equation (19). $\mathbf{T}_{b,v,w}$, if multiplied by \mathbf{p} , will zero out all \mathbf{p}_{b,w^*} except for $\mathbf{p}_{b,w}$, which gets moved to the appropriate spot for $\mathbf{p}_{b,v}$. In its definition, the functions $\mathbf{1}_{(\cdot)}$ are indicator functions for the events within the parentheses. $\mathbf{R}_{(V)}$ is a larger version of the matrix $\mathbf{R}_{(M)}$ used for the means.

$$\mathbf{T}_{b,v,w} = \begin{bmatrix} \mathbf{1}_{(b=1 \cap v=1 \cap w=1)} I_K & \mathbf{1}_{(b=1 \cap v=1 \cap w=2)} I_K & \cdots & \mathbf{0}_{K \times K} \\ \mathbf{1}_{(b=1 \cap v=2 \cap w=1)} I_K & \mathbf{1}_{(b=1 \cap v=2 \cap w=2)} I_K & \cdots & \mathbf{0}_{K \times K} \\ \vdots & \vdots & \ddots & \vdots \\ \mathbf{0}_{K \times K} & \mathbf{0}_{K \times K} & \cdots & \mathbf{1}_{(b=B \cap v=V \cap w=V)} I_K \end{bmatrix} \quad (18)$$

$$\mathbf{R}_{(V)} = \begin{bmatrix} I_{KV} & -I_{KV} & \cdots & \mathbf{0}_{KV \times KV} & \mathbf{0}_{KV \times KV} \\ -I_{KV} & 2I_{KV} & \cdots & \mathbf{0}_{KV \times KV} & \mathbf{0}_{KV \times KV} \\ \mathbf{0}_{KV \times KV} & -I_{KV} & \cdots & \mathbf{0}_{KV \times KV} & \mathbf{0}_{KV \times KV} \\ \vdots & \vdots & \ddots & \vdots & \vdots \\ \mathbf{0}_{KV \times KV} & \mathbf{0}_{KV \times KV} & \cdots & -I_{KV} & \mathbf{0}_{KV \times KV} \\ \mathbf{0}_{KV \times KV} & \mathbf{0}_{KV \times KV} & \cdots & 2I_{KV} & -I_{KV} \\ \mathbf{0}_{KV \times KV} & \mathbf{0}_{KV \times KV} & \cdots & -I_{KV} & I_{KV} \end{bmatrix} \quad (19)$$

The gradient descent algorithm has a soft constraint for orthonormal bases, but we implement a hard constraint for normality as well. After the gradient

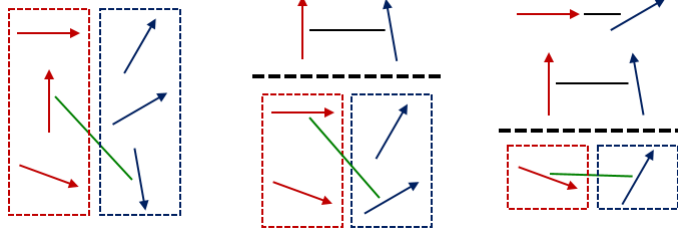


Figure 3: Example Reordering and Sign Change of Initial Basis Vectors

descent algorithm for \mathbf{p} completes, we rescale each basis vector $\mathbf{p}_{b,v}$ to have a unit norm. We cannot similarly force orthogonality without undoing the gradient descent algorithm’s attempts to enforce smoothness.

3.3. Learning Coefficient Vectors

If one differentiates the energy function with respect to a single observation’s coefficient vector β_i and sets this derivative equal to the zero vector, one can obtain the estimate $\hat{\beta}_i$ below for a coefficient vector β_i .

$$\hat{\beta}_i = [\mathbf{P}(\theta_i)]^{-1} [\mathbf{x}_i - \boldsymbol{\mu}(\theta_i)] \quad (20)$$

This inverse is applied to a much smaller matrix than that inverted to find $\hat{\boldsymbol{\mu}}$, so we use a linear system solution to obtain $\hat{\beta}_i$, even with high-dimensional data.

3.4. Initialization

PPCA finds an appropriate local minimum within the energy function, so an appropriate initialization is important for finding a local minimum that can perform similarly to the global minimum. We initialize PPCA using a procedure similar to IPCA, which runs PCA on groups made by binning the parameter θ . We calculate initial mean vectors $\hat{\boldsymbol{\mu}}_{(0),b}$ using Equation (21), which is like a weighted version of the mean calculation from IPCA.

$$\hat{\boldsymbol{\mu}}_{(0),b} = \frac{\sum_{i=1}^n w_{b,i} \mathbf{x}_i}{\sum_{i=1}^n w_{b,i}} \quad (21)$$

To find the initial basis vectors, we choose overlapping subsets of the observations \mathbf{x}_i and assign one subset to each bin endpoint b . The included observations

are all with weight values $w_{b,i}$ above a given threshold such as 0.001. We run PCA on each of these subsets, except that we use the means $\hat{\boldsymbol{\mu}}_{(0),b}$ instead of recalculating the means based on the subsets of \mathbf{x}_i . We then reorder these PCA basis vectors to promote smoothness, using a greedy algorithm. One can start with the first bin endpoint’s basis as the first reference basis, and reorder the bases from the second until the last bin endpoint. Alternatively, one can make the last bin endpoint’s basis the first reference basis, and reorder the bases from the second-to-last until the first bin endpoint.

For each pair of bin endpoints, one first calculates the absolute values of the dot products between each pair of basis vectors using one from each endpoint. The two vectors with the highest absolute value of the dot product are paired, and the sign is inverted for the vector from the basis to reorder if the dot product is negative. This procedure continues, each time only using vectors that are not in any pairs, until all vectors in the reference basis have been paired. If any vectors remain in the basis to reorder, they are assigned to any unused locations. The basis just reordered then becomes the reference basis, the next basis in the order is assigned to be reordered, and the procedure continues until all bases except the original reference have been reordered. The coefficients can then be initialized from the initial mean and basis vectors using Equation (20).

3.5. Putting it all together

The complete PPCA training algorithm is summarized in Algorithm 1.

3.6. Tuning of Parameters

The energy must be tracked, so one can use its path to choose the number of overall cycles n_c , the learning rates (α_m for means, α_v for bases), the number of iterations with those learning rates (n_m for means, n_v for bases), and the non-orthonormality penalty coefficient λ_o . If one wants to choose appropriate roughness penalty coefficients ($\lambda_{r,m}$ for means, $\lambda_{r,v}$ for bases), then one should tune them using a validation set selected randomly from the training examples. Typically, λ_o should be much larger than $\lambda_{r,v}$. However, α_v must decrease as λ_o increases, so an excessively large λ_o leads to unnecessary increases in run-time.

Algorithm 1 PPCA training algorithm

```
1: set  $w_l(\theta_i)$  and  $w_u(\theta_i)$ ,  $i = \overline{1, n}$  using Equation (1)
2: for  $b = 1$  to  $B$  do
3:   initialize  $\hat{\mu}_b$  using Equation (21)
4:   initialize vectors  $\hat{p}_{b,v}$  using PCA on examples with  $w_{b,i} > \epsilon$ 
5:   rearrange vectors  $\hat{p}_{b,v}$  for same  $b$  and switch signs if necessary
6: end for
7: initialize  $\hat{\beta}_i$ ,  $i = \overline{1, n}$  using Equation (20)
8: find  $E_0$  using Equation (4)
9: for  $c = 1$  to  $n_c$  do
10:  update  $\hat{\mu}$  using Equation (9) or gradient descent with Equation (13)
11:  update  $\hat{p}$  using gradient descent with Equation (16)
12:  update  $\hat{\beta}_i$ ,  $i = \overline{1, n}$  using Equation (20)
13:  find  $E_c$  using Equation (4)
14:  if  $E_c > E_{c-1}$  then
15:    break
16:  end if
17: end for
```

4. Modifications and Generalizations for Real Applications

This section details two modifications for generalizations that allow dimensions to vary with the PPCA parameter. The first is for the dimension of the manifold, and the second is for the observations.

4.1. Generalization to Varied Manifold Dimension

For some applications, the manifold dimension can vary with the parameter θ . In Section 5.2, we present such a case, in which higher values of θ are thought to require a more complex representation (with a larger coefficient vector β_i). In this case, each bin endpoint b would have V_b basis vectors, and V would be set to the largest V_b . One would still allocate V basis vectors in \mathbf{p} for each bin endpoint, but one would set $\mathbf{p}_{b,v}$ to be a zero vector if $v > V_b$.

$$E_{\text{rough.}}(\boldsymbol{\mu}, \mathbf{p}, \lambda_{r,m}, \lambda_{r,v}) = \frac{\lambda_{r,m}}{B-1} \sum_{b=1}^{B-1} \|\boldsymbol{\mu}_b - \boldsymbol{\mu}_{b+1}\|^2 + \frac{\lambda_{r,v}}{B-1} \sum_{b=1}^{B-1} \sum_{v=1}^{\min(V_b, V_{b+1})} \|\mathbf{p}_{b,v} - \mathbf{p}_{b+1,v}\|^2 \quad (22)$$

If one has differently-sized bases, the energy component $E_{\text{rough.}}$ needs to follow Equation (22) instead of Equation (7). Also, the energy component $E_{\text{ortho.}}$ needs to follow Equation (23) instead of Equation (8).

$$E_{\text{ortho.}}(\mathbf{p}, \lambda_o) = \lambda_o \sum_{b=1}^B \sum_{v=1}^{V_b} \sum_{w=v}^{V_b} (\langle \mathbf{p}_{b,v}, \mathbf{p}_{b,w} \rangle - \mathbf{1}_{(v=w)})^2 \quad (23)$$

The only three changes to these two equations are to the upper boundaries of summations. In Equation (22), the third summation ends at $\min(V_b, V_{b+1})$ rather than at V . This is intended so PPCA only enforces similarity between the corresponding basis vectors for adjacent bin endpoints if the basis vectors exist for both. In Equation (23), the second and third summations end at V_b instead of at V . This is because there are no vectors beyond vector V_b upon which to enforce orthonormality.

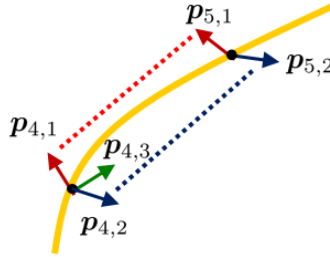


Figure 4: Example of Varied Number of Basis Vectors

In Section 3.4, we detailed a procedure of rearranging initial basis vectors produced by PCA. If the number of basis vectors is either non-decreasing or non-increasing with respect to the bin endpoint number, then this procedure still works, with one modification. If all bin endpoints use V basis vectors, the user has the choice of reordering from the second until the last bin endpoint, or from the second-to-last until the first bin endpoint. However, if the first bin

endpoint's basis is smaller than the last bin endpoint's basis, the reordering procedure must go from the second basis to the last. If the last bin endpoint's basis is smaller than the first bin endpoint's basis, the reordering procedure must go from the second-to-last basis to the first. If the number of basis vectors both increases and decreases when going from the first to the last bin endpoint, then the reordering must be done more manually.

4.2. Generalization to Varied Manifold Ambient Space

Applications also exist in which the manifold ambient space varies with the parameter θ . Section 5.4 demonstrates an example of this sort, using face images. In these data, certain pixels may be considered outside the face shape for a given face. Like the observations, the mean and basis vectors for bin endpoint b may not use all K elements. As shown in Figure 5, we want the mean vectors $\boldsymbol{\mu}_b = (\mu_{b,1}, \dots, \mu_{b,K})^T$ to have similarity enforced between elements $\mu_{b,k}$ and $\mu_{b+1,k}$ only if element k is relevant for both bin endpoint b and bin endpoint $b+1$. So, we create the indicator variables $m_{b,k}$ which equal one if element k is included for bin endpoint b , and zero otherwise. From these, we can construct matrices $\mathbf{M}_{(1),b}$ that can adjust mean vectors $\boldsymbol{\mu}_b$ or basis vectors $\mathbf{p}_{b,v}$, setting unused elements to zero. We also construct matrices $\mathbf{M}_{(R1),b}$ as shown in Equation (25), which can similarly adjust larger vectors.

$$\mathbf{M}_{(1),b} = \begin{bmatrix} m_{b,1} & 0 & \cdots & 0 \\ 0 & m_{b,2} & \cdots & 0 \\ \vdots & \vdots & \ddots & \vdots \\ 0 & 0 & \cdots & m_{b,K} \end{bmatrix}_{K \times K} \quad (24)$$

$$\mathbf{M}_{(R1),b} = \begin{bmatrix} \mathbf{M}_{(1),b} & \mathbf{0}_{K \times K} & \cdots & \mathbf{0}_{K \times K} \\ \mathbf{0}_{K \times K} & \mathbf{M}_{(1),b} & \cdots & \mathbf{0}_{K \times K} \\ \vdots & \vdots & \ddots & \vdots \\ \mathbf{0}_{K \times K} & \mathbf{0}_{K \times K} & \cdots & \mathbf{M}_{(1),b} \end{bmatrix}_{KV \times KV} \quad (25)$$

For each bin endpoint b , one would then calculate $\mathbf{M}_{(2),b} = \mathbf{M}_{(1),b} \mathbf{M}_{(1),b+1}$ and $\mathbf{M}_{(R2),b} = \mathbf{M}_{(R1),b} \mathbf{M}_{(R1),b+1}$. $\mathbf{M}_{(2),b}$ can then be used to adjust the energy

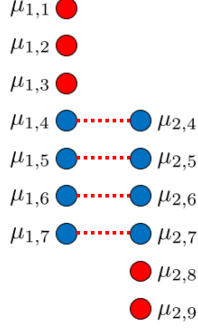


Figure 5: Example of Mean Vectors from Two Endpoints of Same Bin, in Scenario with Varied Ambient Space of Manifold

component E_{rough} as shown in Equation (26). The only adjustments made relative to Equation (7) are two additions of $\mathbf{M}_{(2),b}$.

$$E_{\text{rough}}(\boldsymbol{\mu}, \mathbf{p}, \lambda_{r,m}, \lambda_{r,v}) = \frac{\lambda_{r,m}}{B-1} \sum_{b=1}^{B-1} \|\mathbf{M}_{(2),b}(\boldsymbol{\mu}_b - \boldsymbol{\mu}_{b+1})\|^2 + \frac{\lambda_{r,v}}{B-1} \sum_{b=1}^{B-1} \sum_{v=1}^V \|\mathbf{M}_{(2),b}(\mathbf{p}_{b,v} - \mathbf{p}_{b+1,v})\|^2 \quad (26)$$

The matrices $\mathbf{R}_{(M)}$ and $\mathbf{R}_{(V)}$ from Equations (9), (13), and (16) must be modified as well. These each still have three diagonals that can have non-zero elements, but these diagonals incorporate the indicator variables $m_{b,k}$ and thus can have zeros. The modified versions, shown in Equations (27) and (28), only differ from Equations (12) and (19) by including $\mathbf{M}_{(2),b}$ and $\mathbf{M}_{(R2),b}$, respectively, instead of identity matrices of the same size.

$$\mathbf{R}_{(M)} = \begin{bmatrix} \mathbf{M}_{(2),1} & -\mathbf{M}_{(2),1} & \cdots & \mathbf{0}_{K \times K} & \mathbf{0}_{K \times K} \\ -\mathbf{M}_{(2),1} & \mathbf{M}_{(2),1} + \mathbf{M}_{(2),2} & \cdots & \mathbf{0}_{K \times K} & \mathbf{0}_{K \times K} \\ \mathbf{0}_{K \times K} & -\mathbf{M}_{(3),2} & \cdots & \mathbf{0}_{K \times K} & \mathbf{0}_{K \times K} \\ \vdots & \vdots & \ddots & \vdots & \vdots \\ \mathbf{0}_{K \times K} & \mathbf{0}_{K \times K} & \cdots & -\mathbf{M}_{(2),B-2} & \mathbf{0}_{K \times K} \\ \mathbf{0}_{K \times K} & \mathbf{0}_{K \times K} & \cdots & \mathbf{M}_{(2),B-2} + \mathbf{M}_{(2),B-1} & -\mathbf{M}_{(2),B-1} \\ \mathbf{0}_{K \times K} & \mathbf{0}_{K \times K} & \cdots & -\mathbf{M}_{(2),B-1} & \mathbf{M}_{(2),B-1} \end{bmatrix} \quad (27)$$

$$\mathbf{R}_{(V)} = \begin{bmatrix} \mathbf{M}_{(R2),1} & -\mathbf{M}_{(R2),1} & \cdots & \mathbf{0}_{KV \times KV} \\ -\mathbf{M}_{(R2),1} & \mathbf{M}_{(R2),1} + \mathbf{M}_{(R2),2} & \cdots & \mathbf{0}_{KV \times KV} \\ \mathbf{0}_{KV \times KV} & -\mathbf{M}_{(R2),2} & \cdots & \mathbf{0}_{KV \times KV} \\ \vdots & \vdots & \ddots & \vdots \\ \mathbf{0}_{KV \times KV} & \mathbf{0}_{KV \times KV} & \cdots & \mathbf{0}_{KV \times KV} \\ \mathbf{0}_{KV \times KV} & \mathbf{0}_{KV \times KV} & \cdots & -\mathbf{M}_{(R2),B-1} \\ \mathbf{0}_{KV \times KV} & \mathbf{0}_{KV \times KV} & \cdots & \mathbf{M}_{(R2),B-1} \end{bmatrix} \quad (28)$$

5. Experiments

We evaluated PPCA on four datasets. One had data created from known parameters, so we could ensure that PPCA could recover these true parameters well. The other three were for applications of PPCA to real data: shapes for lymph nodes of varied sizes, appearances for faces of varied blurriness, and appearances for faces of varied yaw rotation.

5.1. Simulation Experiments

First, we tested PPCA's ability to recover a true model, using three-dimensional data created from known mean and basis vectors. These were based on smooth functions of a known parameter θ , defined on the range from 0 to 360. We used 45 observations with $\theta = 4, 12, 20, \dots, 356$. The data were based on two basis vectors and on coefficients drawn independently from a $U(-1, 1)$ distribution. We also added random noise to each element, using a $U(-1.5, 1.5)$ distribution. The formulas for the true mean vectors $\boldsymbol{\mu}(\theta)$ and true basis vectors $\mathbf{p}_1(\theta)$ and $\mathbf{p}_2(\theta)$ were as follows.

$$\boldsymbol{\mu}(\theta) = \left\{ \sin\left(\frac{7\pi\theta}{720}\right), -\frac{91\theta}{1800} + 8, \sin\left(\frac{7\pi\theta}{576} + 0.6\right) \right\}^T \quad (29)$$

$$\mathbf{p}_1(\theta) = \left\{ \sin\left(\frac{7\pi\theta}{1080} + 0.4\right), \tan\left(\frac{7\pi\theta}{4860} - 0.8\right), \frac{49\theta}{1800} - 1.1 \right\}^T \quad (30)$$

$$\mathbf{p}_2(\theta) = \left\{ \cos\left(\frac{7\pi\theta}{972}\right), \cos\left(\frac{7\pi\theta}{576} - 0.4\right), \frac{7\theta}{600} + 1.4 \right\}^T \quad (31)$$

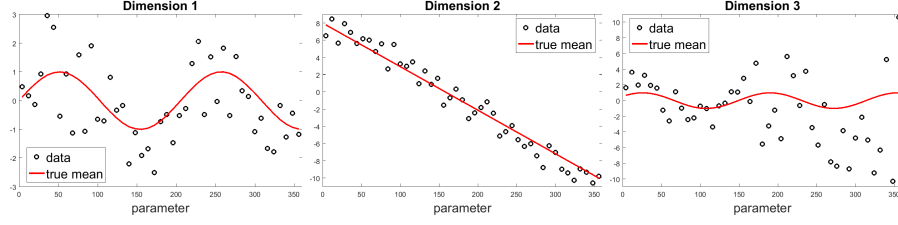


Figure 6: Artificial Data by Element, Compared with True Mean Function

We divided the acceptable parameter range into 14 equally-sized bins. Because the data and model were small (three dimensions and two basis vectors), we could use the analytical solution to calculate the mean vectors and only needed gradient descent for the bases. We used various roughness penalty coefficients, but always used $\lambda_o = 20$, $n_c = 1000$, $n_v = 500$, and $\alpha_v = 0.0001$.

Figure 7 shows the sum of squared ℓ_2 norms for the error in PPCA's and IPCA's estimates of the mean vector, compared to the true mean vectors $\mu(\theta)$. This uses various $\lambda_{r,m}$ but fixes $\lambda_{r,v} = 4.2$. For the bases, we could not use a simple ℓ_2 error because a proper recovery could have the same span, but different vectors and coefficients. We instead measured the ℓ_2 norms of the normal vectors from the planes created by the recovered basis vectors to each of the true basis vectors. Figure 7 shows the sums (across the observations and two true vectors) of these squared ℓ_2 distances. This uses various $\lambda_{r,v}$ but fixes $\lambda_{r,m} = 0.008$.

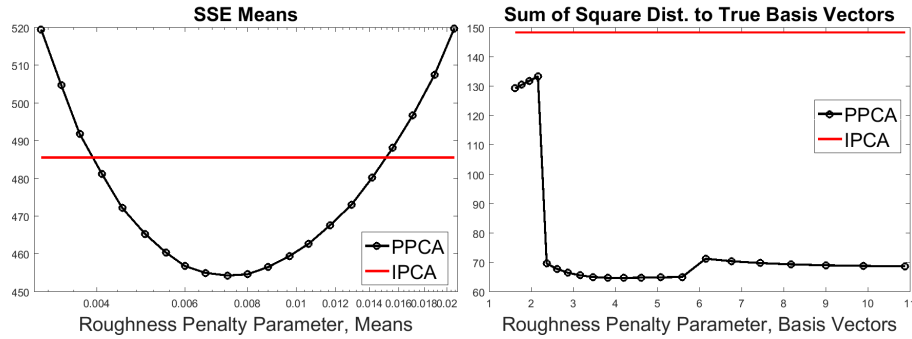


Figure 7: Sum of Squared ℓ_2 Errors for Elements of Artificial Data's Mean Vectors (Left) and Sum of Squared ℓ_2 Distances to Artificial Data's True Basis Vectors (Right)

5.2. Lymph Node Segmentation

Lymph nodes are organs that are part of the circulatory system and the immune system, which are important for the diagnosis and treatment of cancer and other medical conditions. For cancer patients, one may want a segmentation for targeting radiation or for volume estimates. Lymph node sizes generally increase with the onset of cancer, and decrease as treatment succeeds, so volume estimates are used to assess the efficacy of treatment. Generally, radiologists use 3D computed tomography (CT) to assess lymph nodes, and lymph nodes tend to have spherical, elliptical, and bean-like shapes. However, their shape can become more complicated as their size increases. Barbu et al. (2012) demonstrated a model for representing lymph nodes by the lengths of radii, which extend in 162 pre-determined directions from the lymph node’s center [1]. We reduce this 162-dimensional representation of a lymph node’s shape even further, using PPCA and IPCA with 10 or fewer dimensions.

We had a dataset available, in which an experienced radiologist had manually segmented 592 lymph nodes from various patients treated at the National Institutes of Health Clinical Center. We used only the 397 lymph nodes for which the 162-dimensional model was most appropriate. We eliminated 182 lymph nodes which were part of conglomerates of lymph nodes, and 16 for which the radial model’s Sørensen-Dice coefficient was less than 0.8. We then randomly selected 79 lymph nodes to be in the test set, and assigned the remaining 318 lymph nodes to the training set.

The parameter of interest for this application was the lymph node’s diameter, because lymph nodes’ sizes are related to the types of shapes they can take. We used an estimated diameter based on the 162 modeled radii. We divided the lymph nodes into bins of 6-12, 12-18, 18-24, and 24-43 millimeters. The dataset had 55, 156, 77, and 30 training examples per bin and 16, 39, 17, and 7 test examples per bin, in increasing order of bin. We used 3, 5, 7, and 9 basis vectors, respectively, for the IPCA bins, and 2, 4, 6, 8, and 10 basis vectors for the PPCA bin endpoints. These were chosen to allow more shape complexity for the larger lymph nodes, and to ensure that PPCA and IPCA could be compared fairly,

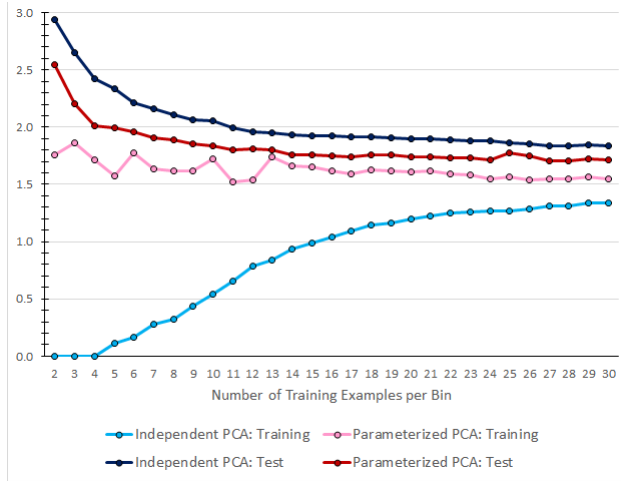


Figure 8: Mean RMSE for Projection of Radial Representation of Lymph Nodes, Evaluated on Training and Test Sets Using Varied Numbers of Training Examples

with the same average dimensions used per bin.

We evaluated PPCA and IPCA after fitting the models using different numbers of training examples per bin, from 2 to 30. These smaller training sets were chosen randomly from the full training set. All smaller training sets were subsets of the larger training sets, to ensure a more valid comparison of the effect of the training set size. Each time, we calculated the root mean squared error (RMSE) of the projection of each lymph node’s 162-dimensional vector of radii, and then found the mean across the lymph nodes of the training or test set. For PPCA, we used gradient descent algorithms for both the mean and basis vectors. We used $\lambda_{r,m} = 0.007$, $\lambda_{r,v} = 30,000$, $\lambda_o = 10^7$, $n_c = 200$, $n_m = 100$, $n_v = 100$, $\alpha_m = 0.01$, and $\alpha_v = 10^{-8}$.

Figure 8 shows that IPCA overfit the data compared to PPCA, particularly for smaller training sets. For all tested sizes, PPCA had noticeably higher error than IPCA when projecting the training set, but noticeably lower error than IPCA did when projecting the test set.

5.3. Facial Images with Blur

Modeling images of human faces in photos or video frames is useful for creating novel images that satisfy the constraints of realistic faces, such as for

animation. It can also modify a known face to show poses or expressions not in available images. Face models can be used as generative face detectors, too, with applications such as auto-focusing a camera or detecting intruders on a security camera. Face modeling can also aid face recognition, by aligning the images to be recognized or by providing the lower-dimensional representation that can be matched against a dictionary.

Variations in the conditions (such as illumination) of images present challenges for face models. One such variation is the blurriness of photographs. Digital cameras, particularly those in many mobile phones, are used frequently to produce photos that may not be appropriately sharp. Even professional photographers using high-grade cameras can produce images with blurred faces in the background. The blurriness of a facial image changes one’s expectations for the face’s appearance, as well as the types of variation in the appearance, so we modeled facial images using a parameter based on blurriness.

To quantify blurriness, we assumed that a Gaussian blur filter could approximate the transformation from an unobserved, unblurred image to the observed, blurred image. This Gaussian blur is a convolution using the kernel $K(x, y|\sigma)$ from Equation (32), where x is the horizontal distance and y is the vertical distance between the two pixels involved. We used σ from Equation (32) (with $\sigma = 0$ for an unblurred image) as the PPCA parameter, because higher values of σ create blurrier images.

$$K(x, y|\sigma) = \frac{1}{2\pi\sigma^2} \exp\left(-\frac{x^2 + y^2}{2\sigma^2}\right) \quad (32)$$

We treated the facial images from the CBCL Face Database #1 [11] as unblurred, and added Gaussian blur with a 7×7 kernel and varied σ . The database had 472 faces chosen as the test set, and the remaining 2,429 as the training set. We used three bins for σ : 0-1, 1-2, and 2-3. The training and test images were created from the original faces such that each original face produced one blurred image for each of the three bins. The parameter σ for each observation was selected randomly from a $U(0, 1)$, $U(1, 2)$, or $U(2, 3)$ distribution, depending on which bin’s image was being produced.

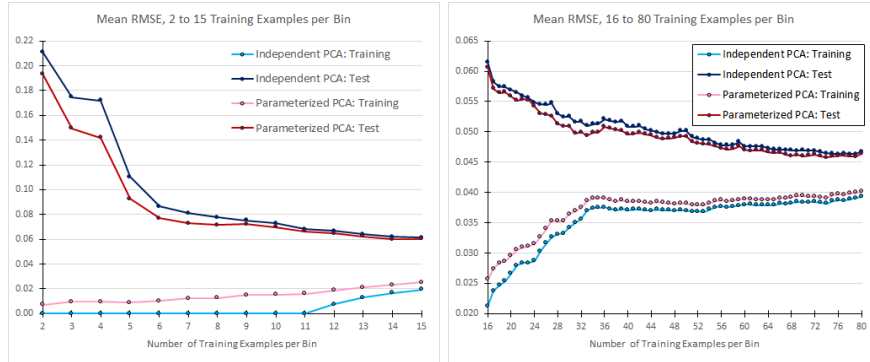


Figure 9: Mean RMSE for Projection of Test Set Blurred Facial Images, Using Varied Numbers of Training Examples (Left: 2-15, Right: 16-80)

We used 10 basis vectors for each IPCA bin or PPCA bin endpoint. For PPCA, we used gradient descent for both the mean and basis vectors. We used $\lambda_{r,m} = 0.6$, $\lambda_{r,v} = 2$, $\lambda_o = 1000$, $n_c = 300$, $n_m = 100$, $n_v = 100$, $\alpha_m = 0.01$, and $\alpha_v = 0.0001$. The training set varied from 2 to 80 examples per bin. For all sizes of training set, all bins had images made from the same faces, but had different added blur according to the values σ . The smaller training sets were always subsets of the larger training sets, to allow for better examination of the effect of the training set size. Figure 9 shows the mean across training or test set images for the RMSE of the blurred images’ projections. PPCA had lower projection error on the test set than IPCA for each training size from 2 to 80 examples per bin, but had a more noticeable advantage when both methods used eight or fewer training examples per bin.

5.4. Facial Images with Rotation

Section 5.3 addressed the challenges of modeling facial images with different levels of blurriness. A separate challenge in face modeling is out-of-plane rotation, which changes the expected appearance of facial features and produces predictable changes in the occlusion of important facial features. Yaw rotation is highly prevalent in photos, particularly for “in the wild” photos, which are those taken in uncontrolled settings, often by ordinary users. One could model pitch or roll rotation instead using PPCA, but we focus on yaw rotation because

it has the largest variation in available face images.

5.4.1. Background

Linear models for facial appearances exist, such as active appearance models (AAMs) [4] and 3D morphable models (3DMMs) [2]. AAMs typically incorporate in-plane rotation and suffer from an inability to model out-of-plane rotation, but 3DMMs exist in 3D and can use 3D rotation. 3DMMs can be fit to 2D test images, but they are trained using 3D facial scans performed in a laboratory setting. Potential users typically do not have the necessary equipment for these scans, and even with the equipment, one has very limited training data relative to a dataset of 2D images. Furthermore, applications for in-the-wild images grow as these images become more important for social media and other Internet uses, and the laboratory setting on the scan data makes them dissimilar to in-the-wild images. Zhu and Ramanan (2012) showed that training on in-the-wild images greatly increases face detection performance on in-the-wild test data [18], and it seems logical that similarity between training and test data would be desirable for face modeling as well.

Gross, Matthews, and Baker (2004) modify AAMs to address occlusion [7]. This does not distinguish occlusion by an object (such as a hand in front of a face) from self-occlusion caused by out-of-plane rotation, so it does not take advantage of the more predictable nature of rotation-based self-occlusion. Xiao et al. (2004) also modify AAMs, creating a hybrid of a 2D and a 3D model by adding extra parameters and constraints to a 2D model [16]. It allows the training advantages of a 2D model with some of the advantages of a 3D model, but compared to PPCA, it does not address out-of-plane rotation as directly and relies more on 3D elements not directly observable in the 2D data.

AAMs and 3DMMs each incorporate two linear models: one for the shape mesh, and one for the appearance after removing the influence of shape variation. AAMs typically use frontal images only and translate the appearance from the original image’s shape mesh to the mean shape mesh by triangular warping. Yaw rotation creates predictable changes to both the shape and the appearance.

PPCA could model both, but we chose to focus on the appearance component, and modeled the shape using a rigid, 3D shape model built on other data.

5.4.2. Data

We used 272 human facial images from the Annotated Facial Landmarks in the Wild (AFLW) database [9], which includes annotations of the locations and occlusion status of 21 key points. We chose the subset such that the faces were all in color and appeared to be of 272 different people. We used yaw rotation in radians as the PPCA parameter θ . It was limited to the range from -0.5π to 0.5π , and we divided the range into 16 equally-sized bins. Our subset of AFLW had 17 images in each bin, and three images per bin were selected randomly to be in the test set. The remaining 14 images per bin were eligible for training, but we varied the training set size from 2 to 14 images per bin. The smaller training sets were always subsets of the larger training sets. Values of θ came from finding the roll, pitch, and yaw angles that best rotated the rigid shape model to fit the unoccluded key points' horizontal and vertical coordinates. Several yaw angles and key point locations were corrected manually.

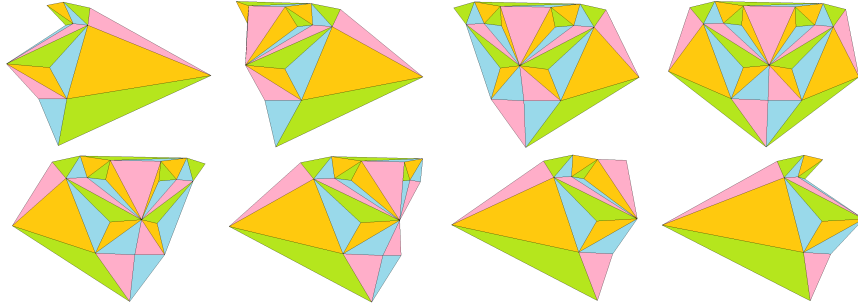


Figure 10: Triangulation at Bin Endpoints 2, 5, 8, 9, 10, 12, 14, and 16

AAMs commonly use a triangulation of the face to translate a shape mesh of key points into a shape that can cover pixels. We also used a triangulation, which we constructed manually to have triangles that are less likely to have one of three vertices occluded at yaw angles from $-\frac{\pi}{2}$ to $\frac{\pi}{2}$. This generally implied triangles that ran more vertically than in automatic triangulation methods. PPCA promotes the smoothness of adjacent bin endpoints, so the

triangles needed to use pixels that corresponded to equivalent areas in other bin endpoints’ shapes. We calculated the triangle’s area for each bin endpoint shape in our 3D model, and used the largest-area version of the triangle for PPCA. We warped each triangle from the original images to these model triangles, which were considered occluded or not based on the direction of the normal vector to that triangle in the rigid shape model rotated to the appropriate yaw angle. AFLW’s image-specific occlusion annotations were not used after estimating θ .

We tested two numbers of basis vectors per bin endpoint, 4 and 10, to determine whether this modeling choice affects the appropriateness of PPCA. IPCA bins used the same number of basis vectors as PPCA bin endpoints did. We also allowed the model to vary based on the presence of whitening. The intensities before whitening were represented as double floating-point numbers from zero (black) to one (white). If whitening were used, each image would get six additional parameters in its representation, which were not a part of PPCA (or IPCA) itself. After warping an image, we stored the original mean intensity and standard deviation for red, green, and blue. We translated and rescaled the intensities such that each color had a mean of 0.5 and a standard deviation of 0.031. The latter was chosen to be just large enough to keep all whitened intensities within the $[0, 1]$ interval. PPCA and IPCA modeled the whitened versions, and after projecting the whitened image, we reversed the whitening transformation using the image-specific means and standard deviations by color.

5.4.3. Model Fitting and Results

We trained models with training set sizes from 2 to 14 examples per bin. PPCA needed to use gradient descent to optimize both the mean and basis vectors. We used $\lambda_{r,m} = 0.001$, $\lambda_{r,v} = 0.01$, $\lambda_o = 1000$, $n_c = 200$, $n_m = 100$, $n_v = 250$, $\alpha_m = 0.0001$, and typically $\alpha_v = 10^{-6}$. The models with two to four training examples per bin and 10 basis vectors required smaller α_v to avoid divergence. The occlusion of each triangle was considered known, because it was treated as a function of a known yaw angle. So, we set the image-specific mean vector and basis vectors in IPCA and PPCA projections to have zeros for

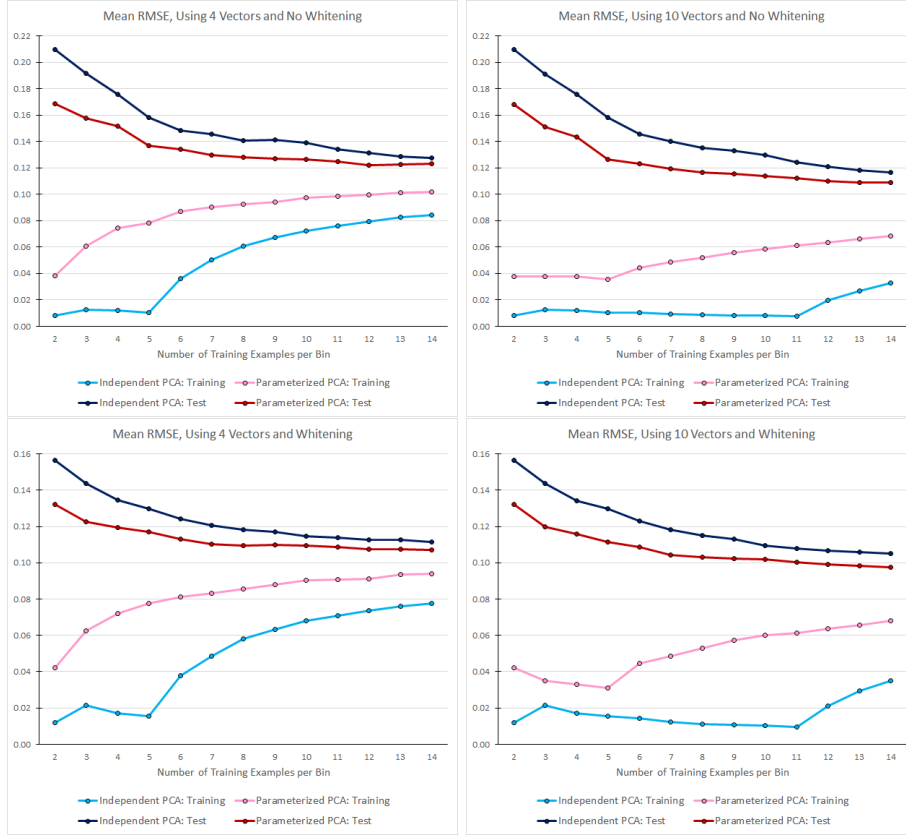


Figure 11: Mean RMSE for Projection of Facial Images with Yaw Rotation Parameter, Evaluated on Training and Test Sets Using Varied Numbers of Training Examples

any out-of-shape pixels before we found images' coefficients. After projecting the image and reversing whitening if it was used, we calculated the RMSE for each image in the training and test sets.

Figure 11 shows the means of these RMSEs, which are averaged across the images of the training or test set. For all four styles of fitting the models and for all training set sizes tested, IPCA overfits the data relative to PPCA. PPCA has higher error on the training set but lower error on the test set than IPCA does. The difference is even more noticeable when we use eight or fewer training examples per bin.

Figure 12 shows the IPCA and PPCA mean vectors, warped to the bin midpoint (IPCA) or bin endpoint (PPCA) shapes. These models used four



Figure 12: Mean Facial Images by Rotation-Based Bin (or Bin Endpoint) for IPCA (Left) and PPCA (Right), Using No Whitening

vectors per bin (or bin endpoint), no whitening, and 12 training examples per bin. The IPCA means appear to treat characteristics of the training images as characteristics of the bin to a higher degree than the PPCA means do. One can see more noticeable changes from bin to bin for IPCA with respect to eye color and shape, lip color, illumination, and skin complexion. The smoothness of the mean shape can be improved further for PPCA by increasing the penalty $\lambda_{r,m}$ to 0.1, as shown in Figure 13. We did not test additional training set sizes with $\lambda_{r,m} = 0.1$, but for this example, the mean RMSE for the test set (0.1220) was effectively the same as for $\lambda_{r,m} = 0.001$ (mean RMSE = 0.1220). Both had lower mean RMSEs for projection error than IPCA (0.1313) did.



Figure 13: Mean Facial Images by Rotation-Based Bin Endpoint for PPCA, Using Higher Roughness Penalty and No Whitening

6. Conclusion and Future Direction

We have presented a novel method, parameterized principal component analysis (PPCA), for modeling multidimensional data on linear manifolds that vary smoothly according to a contextually important parameter θ . We compared PPCA to independent principal component analysis (IPCA), the use of separate principal component analysis models for groups formed by values of the parameter θ . We showed that PPCA outperformed IPCA at recovering known true mean vectors and true basis vectors based on smooth functions of the parameter θ , and at producing lower projection error on three datasets. These datasets contained lymph node shapes that varied by the diameter, blurred human facial images that varied by the standard deviation σ of the Gaussian blur applied, and human facial images that varied by the angle of yaw rotation. In each of the three datasets, PPCA’s performance on the test set was the strongest relative to IPCA when the two methods used smaller training sets.

We have explored three types of applications of PPCA to datasets, with different types of parameter in each. However, many other applications exist and future work could extend PPCA to more parameters than the three we tested. Also, we performed some investigation of different modeling choices when modeling faces with different yaw rotation, but it would be beneficial to have further tests of how different numbers of basis vectors used and different adjustments to the data affect the utility of PPCA.

References

References

- [1] Adrian Barbu, Michael Suehling, Xun Xu, David Liu, S Kevin Zhou, and Dorin Comaniciu. Automatic detection and segmentation of lymph nodes from ct data. *Medical Imaging, IEEE Transactions on*, 31(2):240–250, 2012.
- [2] Volker Blanz and Thomas Vetter. A morphable model for the synthesis of 3d faces. In *Proceedings of the 26th annual conference on Computer*

- graphics and interactive techniques*, pages 187–194. ACM Press/Addison-Wesley Publishing Co., 1999.
- [3] Songcan Chen and Tingkai Sun. Class-information-incorporated principal component analysis. *Neurocomputing*, 69(1):216–223, 2005.
 - [4] Timothy F Cootes, Gareth J Edwards, and Christopher J Taylor. Active appearance models. *IEEE Transactions on pattern analysis and machine intelligence*, 23(6):681–685, 2001.
 - [5] Fernando De la Torre and Takeo Kanade. Multimodal oriented discriminant analysis. In *Proceedings of the 22nd international conference on Machine learning*, pages 177–184. ACM, 2005.
 - [6] Andrew B Goldberg, Xiaojin Zhu, Aarti Singh, Zhiting Xu, and Robert Nowak. Multi-manifold semi-supervised learning. In *International Conference on Artificial Intelligence and Statistics*, pages 169–176, 2009.
 - [7] Ralph Gross, Iain Matthews, and Simon Baker. Constructing and fitting active appearance models with occlusion. In *Computer Vision and Pattern Recognition Workshop, 2004. CVPRW'04. Conference on*, pages 72–72. IEEE, 2004.
 - [8] Xiaoferi He and Partha Niyogi. Locality preserving projections. In *Neural information processing systems*, volume 16, page 153. MIT, 2004.
 - [9] Martin Koestinger, Paul Wohlhart, Peter M. Roth, and Horst Bischof. Annotated facial landmarks in the wild: A large-scale, real-world database for facial landmark localization, 2011.
 - [10] Aleix M Martínez and Avinash C Kak. Pca versus lda. *Pattern Analysis and Machine Intelligence, IEEE Transactions on*, 23(2):228–233, 2001.
 - [11] MIT Center For Biological and Computation Learning. Cbcl face database #1, 2000. Accessed: 2016-04-07.

- [12] Nikolaos Pitelis, Chris Russell, and Lourdes Agapito. Learning a manifold as an atlas. In *Computer Vision and Pattern Recognition (CVPR), 2013 IEEE Conference on*, pages 1642–1649. IEEE, 2013.
- [13] René Vidal, Yi Ma, and Shankar Sastry. Generalized principal component analysis (gpca). In *Computer Vision and Pattern Recognition, 2003. Proceedings. 2003 IEEE Computer Society Conference on*, volume 1, pages I–621. IEEE, 2003.
- [14] Rene Vidal, Yi Ma, and Shankar Sastry. Generalized principal component analysis (gpca). *Pattern Analysis and Machine Intelligence, IEEE Transactions on*, 27(12):1945–1959, 2005.
- [15] Elif Vural and Pascal Frossard. Learning smooth pattern transformation manifolds. *Image Processing, IEEE Transactions on*, 22(4):1311–1325, 2013.
- [16] Jing Xiao, Simon Baker, Iain Matthews, and Takeo Kanade. Real-time combined 2d+ 3d active appearance models. In *CVPR (2)*, pages 535–542, 2004.
- [17] Daoqiang Zhang, Zhi-Hua Zhou, and Songcan Chen. Semi-supervised dimensionality reduction. In *SDM*, pages 629–634. SIAM, 2007.
- [18] Xiangxin Zhu and Deva Ramanan. Face detection, pose estimation, and landmark localization in the wild. In *Computer Vision and Pattern Recognition (CVPR), 2012 IEEE Conference on*, pages 2879–2886. IEEE, 2012.

Ajay Gupta received his B.S. degree in statistics from Case Western Reserve University in 2005 and his M.S. and Ph.D. degrees in statistics from Florida State in 2013 and 2016. His research interests include machine learning, face modeling, financial applications, and neural networks.

Adrian Barbu received his B.Sc. degree from University of Bucharest, Romania, in 1995, a Ph.D in Mathematics from Ohio State University in 2000 and a Ph.D in Computer Science from UCLA in 2005. From 2005 to 2007 he was

a research scientist and later project manager in Siemens Corporate Research, working in medical imaging. He received the 2011 Thomas A. Edison Patent Award with his co-authors for their work on Marginal Space Learning. From 2007 he joined the Statistics department at Florida State University, first as assistant professor, and since 2013 as associate professor. His research interests are in computer vision, machine learning and medical imaging.